## Near-field terahertz imaging of ferroelectric domains in barium titanate

Milan Berta[a]; Filip Kadlec[a]

[a] Fyzikální ústav AV ČR, Czech Republic

## PLEASE SCROLL DOWN FOR ARTICLE

Taylor & Francis
Taylor & Francis Group

# RESEARCH ARTICLE

## Near-field terahertz imaging of ferroelectric domains in barium titanate

Milan Berta and Filip Kadlec*

*Fyzikální ústav AV ČR, v. v. i., Na Slovance 2, CZ-182 21 Praha 8, Czech Republic*

We report on results of a near-field imaging experiment with broadband terahertz pulses applied to a BaTiO$_3$ multidomain single crystal. Data with a spatial resolution below 15 μm were collected by our scanning time-domain terahertz imaging setup. We performed the scanning by an asymmetric skewed sapphire probe metallised from two sides ended with a 60 μm × 140 μm facet. The imaging scans were performed with various angles of the polarisation of the probing field with respect to the direction of the domain walls in order to identify the orientations with optimal sensitivity. The raw experimental data were prewhitened and processed by the singular value decomposition. In this way, independent components belonging to experimental features (polarisation, noise and external perturbations) were found. The spatial resolution of the sensing probe was found significantly higher than that allowed by the outer dimensions of the probe end facet. This result was also confirmed by electromagnetic-field simulations.

## 1. Introduction

For resolving subwavelength features on a surface of a sample, it is necessary to apply a near-field method. Various methods of near-field imaging are available for acquiring a subwavelength resolution in the terahertz (THz) frequency domain. We use a metal-dielectric probe [1], in which the THz radiation is constrained between two separate metal layers guiding the waves into a small volume near the probe end and in the vicinity of a sample surface. The field close to the probe end is enhanced due to the confinement and there is no limitation on low-frequency limit with respect to a cut-off frequency. These are the two main advantages of our confinement approach compared to the other ones currently used, namely, tip-enhanced and aperture-based near-field imaging methods and those involving an optical-laser beam for sensing the near field [2].

The sensitivity of a near-field imaging method is often validated by scanning through a metallic pattern on a non-metallic substrate (dielectric) ensuring a high contrast in the image pattern. However, for potential applications, it is crucial to investigate the imaging capabilities on samples in which contrast in permittivity is lower. With this intention, we demonstrated earlier that our method is able to reveal local anisotropy in ferroelectrics [3].

---

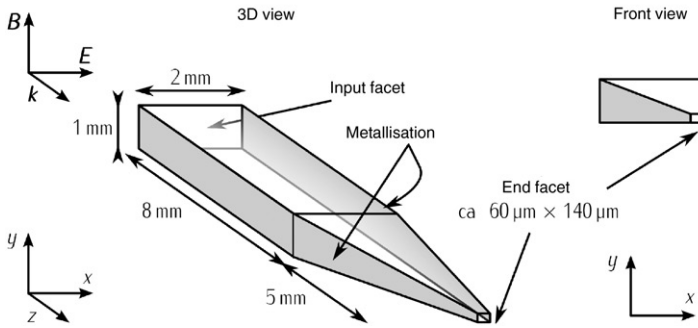*Corresponding author. Email: kadlecf@fzu.cz

Figure 1. A schematic drawing of an asymmetric MDP with two neighbouring sides tapered and with two narrower sides metallised.

In this article, we present results of imaging ferroelectric domains using a confinement method based on pyramidal-shaped sensing probes [1].

## 2. Data acquisition

### 2.1. *The metal-dielectric probe*

The probe is fabricated from a $1\,mm \times 2\,mm \times 15\,mm$ block of sapphire that acts as a low-loss dielectric in THz. One end of the block is skewed from two neighbouring sides to form a quadrilateral truncated oblique frustum, i.e. an asymmetric pyramid with a $60\,\mu m \times 140\,\mu m$ small end facet (Figure 1).

This metal-dielectric probe (MDP) is designed to operate in a reflection mode, therefore it is suitable even for thick samples and for those which are opaque in the THz spectral range. The MDP concentrates the incoming THz waves into a small volume around the end facet without a cut-off frequency. This makes it possible to scale down the geometry – and to increase the spatial resolution this way – while employing a substantial part of the THz wave energy for sensing the sample.

### 2.2. *Experimental setup*

Our setup for the time-domain THz spectroscopy works in the frequency range of 0.1–1.4 THz [3]. Free-space propagating THz pulses are generated using 50 fs long Ti : sapphire laser pulses and a Tera-SED large-area biased photoconductive emitter [4]. A photograph showing the paths in the terahertz part of the setup is shown in Figure 2.

The THz pulses are focused by a pair of plastic lenses and a mirror onto the input facet of the MDP in such a way that the polarisation of the radiation is perpendicular to the metallised surfaces of the MDP. The radiation travels along the probe and the focusing in the frustum is enabled by the metallisation on the two opposite sides. In this way, the electromagnetic field is guided and concentrated into a small volume around the end facet. The focused-field pattern interacts with the close environment of the probe, in which a sample is placed, and a significant part of the radiation is reflected back. These back-reflected pulses are routed by the wire-grid polarisers and plastic lenses onto a 1 mm thick ZnTe [011] crystal. A shielding around the input facet ensures that no radiation travels aside the MDP. The temporal profiles of the electric intensity of the THz pulses $E(t)$ (also called waveforms), in which $t$ is the delay time in the waveform, are detected by electro-optic
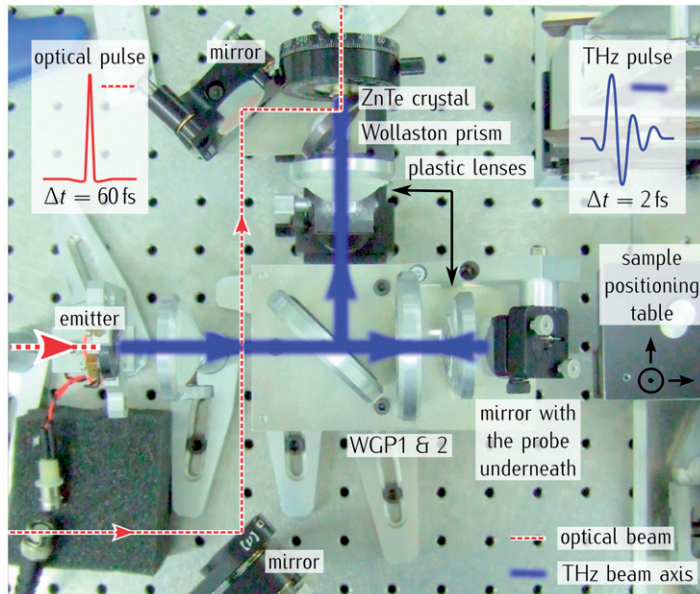
Figure 2. The THz beam generated in the emitter is polarised and routed by two plastic lenses and a mirror into a MDP. The radiation is lead into the detection system introduced by the ZnTe emitter after interacting with a sample on a positioning table.

sampling [5] in the ZnTe crystal. Different materials placed into the proximity of the probe leave different fingerprints in the shape of the output waveforms. During the measurement, 7 ps long waveforms were collected, while the time delay of the collection range corresponds to the time needed by the THz pulse to pass twice through the MDP in its whole length. The manipulation with the sample under the probe is accomplished by using a micro-positioning stage.

### 2.3. *Sample*

Imaging scans were performed on a polished surface of a 1 mm thick barium titanate (BaTiO$_3$) single-crystal platelet. Crystals of this ferroelectrics exhibit a high anisotropy; its refractive indices in the THz frequency range are $n_o \approx 45$, $n_{eo} \approx 7.5$ [6]. For performing imaging, we chose an area with a characteristic inclusion and multiple straight domain stripes (Figure 3). Micro-Raman measurements showed us the orientation of the optical axes as well as that of the polarisation in and aside the domain stripes (see the inset of Figure 3). The in-plane polarisation clearly alters by 90°. The narrower domain stripes of a 4–7 μm width were separated by a few tens to 100 μm wide monodomain gaps. Measurements were performed in four configurations A–D with different orientations of the MDP with respect to the sample features.

### 2.4. *Data decomposition*

Experimental data were collected from areas comprising $m_1 \times m_2$ pixels. At each pixel a 7 ps long waveform with $n$ datapoints was recorded. The data were linearised to $n \times (m_1 \cdot m_2) = n \times m$ matrix datasets and these matrices were processed by the singular
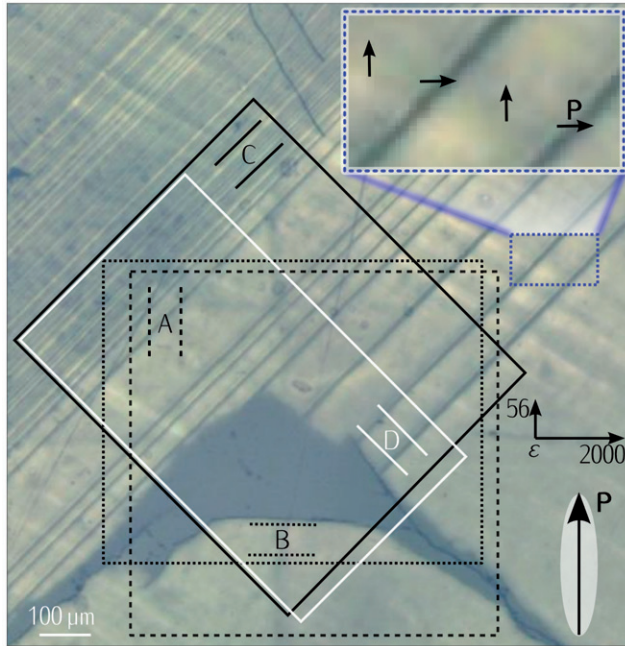
Figure 3. A photograph of the BaTiO$_3$ sample in which four scanning areas (A–D) are sketched with the in-scale pattern of the MDP end-facet metallisation. The dimensions of the probe were $60 \times 140\,\mu m$. The inset (upper right corner) shows the in-plane orientation of the polarisation within the domains.

value decomposition (SVD) [7–9]. The SVD is an orthogonal transformation and makes it possible to separate the useful signal, contributions of experimental artifacts and noise in a large (possibly multivariate) dataset. The R software environment [10] for statistical computing was used to decompose the data employing its svd function.

The linearised sets $E(t, d) \equiv \mathbf{E}$ of experimentally obtained waveforms, in which $t$ is the time delay and $d$ represents the position on the sample, underwent a pretreatment (prewhitening) before the decomposition which allowed an unambiguous comparison of components among all measurements. Therefore, first, we extracted a normalisation factor of the measurement. To this purpose, we calculated the mean values of the rows of the raw dataset $E(t, d)$. The result was an average waveform $e_{\mathrm{mean}}(t)\langle d \rangle$ with $n$ datapoints. That was extended to an $n \times m$ matrix $\mathbf{E}_{\mathrm{mean}}$ containing identical columns which was subtracted from the raw dataset $E(t, d)$ to create a prewhitened matrix $\mathbf{E}_{\mathrm{residual}} = \mathbf{E} - \mathbf{E}_{\mathrm{mean}}$. Both the mean matrix $\mathbf{E}_{\mathrm{mean}}$ and the residual matrix $\mathbf{E}_{\mathrm{residual}}$ were then decomposed by SVD.

The number of components separable by the SVD is $\min(n, m)$. In our case, the collected waveforms contained much less points than the pixel maps, therefore $\min(n, m) \equiv n$ for both matrices. But only the first component has a meaning when decomposing $\mathbf{E}_{\mathrm{mean}}$ (due to the columns identity). The decompositions follow the relations

$$\mathbf{E} - \mathbf{E}_{\mathrm{mean}} = \mathbf{E}_{\mathrm{residual}} \overset{\mathrm{SVD}}{=} \mathbf{ULV}^{\mathrm{T}} = \sum_{j=1}^{n} \lambda_j \mathbf{u}_j \mathbf{v}_j^{\mathrm{T}}, \tag{1}$$

$$\mathbf{E}_{\mathrm{mean}} \overset{\mathrm{SVD}}{\equiv} \lambda_{\mathrm{mean}} \mathbf{u}_{\mathrm{mean}} \mathbf{v}_{\mathrm{mean}}^{\mathrm{T}}. \tag{2}$$

The products of the decomposition in Equation (1) are as follows: $n$ left singular vectors $\mathbf{u}_j$ (lSVs, columns in the unitary matrix denoted $\mathbf{U}$), $n$ right singular vectors $\mathbf{v}_j$ (rSVs, columns of the unitary matrix $\mathbf{V}$) and the same number of singular values $\lambda_j$ (SVs) in the diagonal matrix $\mathbf{L}$ ($\mathbf{L} = \mathrm{diag}\,(\lambda_1, \lambda_2, \ldots, \lambda_n)$). The SVs $\lambda_j$ are the respective weights (or factors) to the lSVs and rSVs. Notation of the products of the SVD is in accordance with a general definition, e.g. [7]. The singular values are ordered in decreasing order: $\lambda_{j+1} < \lambda_j$. The lSVs and rSVs are normalised, i.e. $\|\mathbf{u}_j\| = \sqrt{\mathbf{u}_j \mathbf{u}_j^{\mathrm{T}}} = 1$.

The products of the decomposition in Equation (2), the singular vectors $\mathbf{u}_{\mathrm{mean}}$ and $\mathbf{v}_{\mathrm{mean}}$ and the singular value $\lambda_{\mathrm{mean}}$ were merged into the decomposed matrices $\mathbf{U}$, $\mathbf{V}$ and $\mathbf{L}$ from Equation (1). Usually, the changes during the measurement are subtle and the mean values are high compared to the residuals, therefore this mean component is placed to the first position and indexed $j = 1$. The vectors and value representing the very last noise component (indexed $j = n + 1$ after the merge) were deleted from the dataset to maintain the correct dimensionality of the matrices $\mathbf{U}$, $\mathbf{V}$ and $\mathbf{L}$. The singular values and vectors can be visualised and plotted in arbitrary units in their respective spaces (Figure 4a–c). The $\lambda_{\mathrm{mean}} \equiv \lambda_1$ and $\mathbf{u}_{\mathrm{mean}} \equiv \mathbf{u}_1$ are represented by an open gray circle and a gray dashed line in Figure 4(a) and (b), respectively.

It is sufficient to consider only SVs up to a certain index $j$ as physical processes in the measurement. The scree test [11] was used to select the significant SVs and to reject the so-called noise components – those creating the noise floor. An example of the applied scree test is in Figure 4(a).

## 3. Results and discussion

The detected patterns could be linked to the sample surface features only in two of the four measurement (sample-probe) configurations. In the configuration B, we clearly identified components representing the domain structure besides those belonging to experimental artefacts. We could resolve the domains that were 5–7 μm wide although the probe had a larger width, 60 μm (Figure 4c). Moreover, it is also possible to resolve the domain structure in a time slice of the prewhitened waveforms, e.g. at $t = 190.97$ ps, see Figure 4(e). The difference between the rSV3 component and the time cut at $t = 190.97$ ps is minor (cf. Figure 4c and e), but that is not a rule in other measurements. The reason for this is a strong interaction of the ferroelectric domains with the near-field in this configuration. Therefore, in this case, it would be equally possible to perform such an imaging without the necessity to collect waveforms. Instead, a detection of the THz intensity during the scanning would be done at a fixed delay-time position for which the strongest response was revealed previously (Figure 4b).

In the configurations A and C, we were not able to resolve significant features that could be linked to the sample surface structure. In the case of the configuration C, the projection of the polarisation $\mathbf{P}$ onto the probe-field axis was the same for both types of domains. Therefore, it is presumable that the electromagnetic field at the probe end did not sense any contrast in this case. Surprisingly, even in such a case, we identified components representing a part of the domain structure in the configuration D (Figure 5a). This result was observed, although the projection of polarisation in the sample parallel with that of the near-field should be constant through the whole scanning area. The reason for this was possibly an inhomogeneous field distribution near the probe metallisation end caused by a non-perfect focusing in the probe.
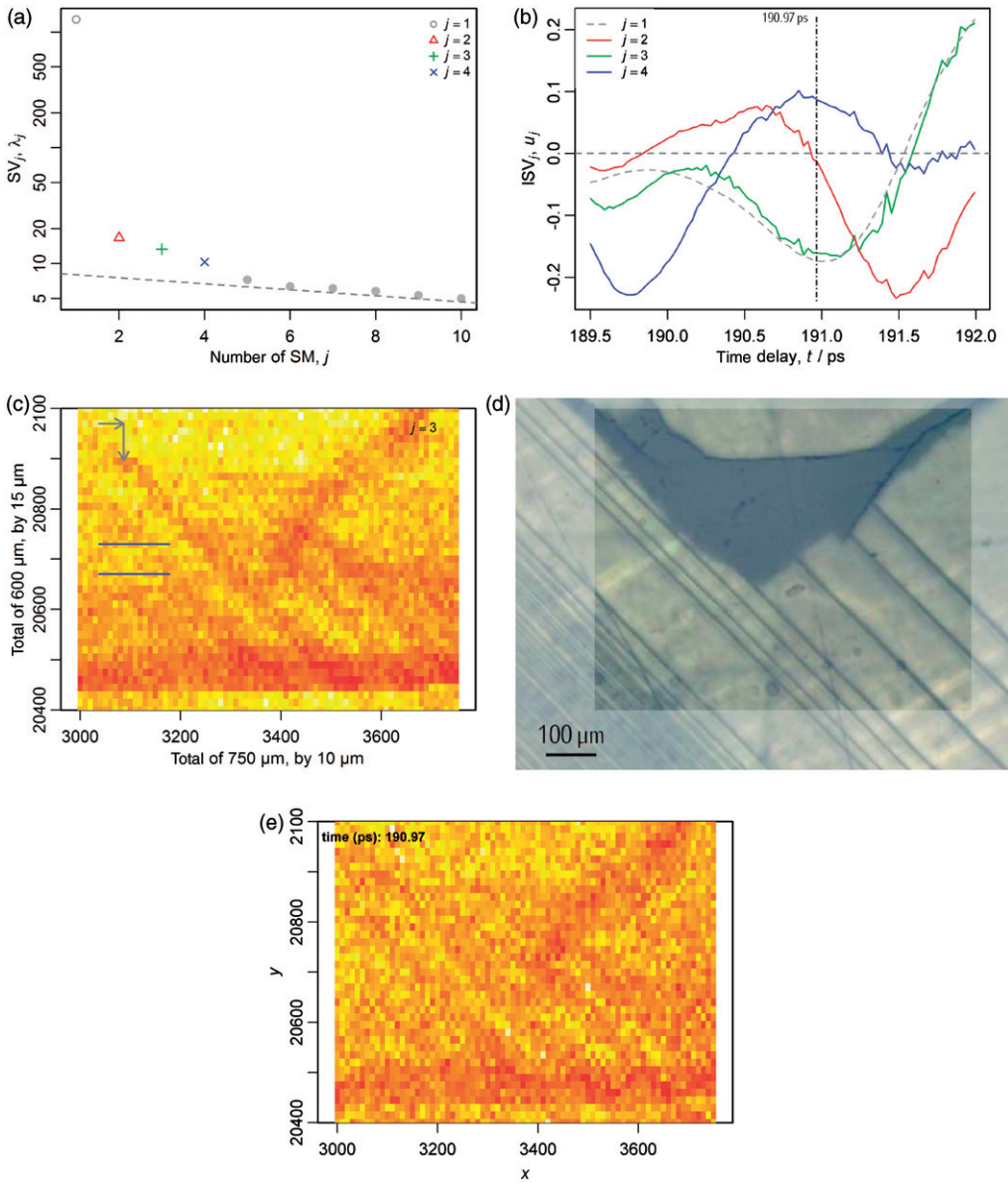
Figure 4. Scanned area B and the SVD products of the dataset. A comparison of the photograph of the scanned area (d) with one of the extracted components (c). The slimmest domains stripes are 5–7 μm wide. (a) The scree test applied on the calculated singular values $\lambda_j$, see Section 2.4. The SV1 is the weight of the averaged waveform obtained at the prewhitening. The SVs for $j > 4$ belong to the noise. (b) The profiles of the independent contributions to the waveform (lSV1–lSV4). The vertical line at $t = 190.97$ ps denotes the time delay for which the intensity is depicted in Figure 4(e). (c) The features in one of the $\mathbf{v}_j$ components (delinearised rSV3) match those on the photograph (Figure 4(d)). The two parallel line segments represent the size and orientation of the sapphire-probe metallisation. (d) A photograph of the scanned area B – a portion of Figure 3 for visual comparison with intensity profiles in Figure 4(c) and 4(e). (e) A profile of the intensity change extracted directly from the prewhitened dataset at $t = 190.97$ ps.
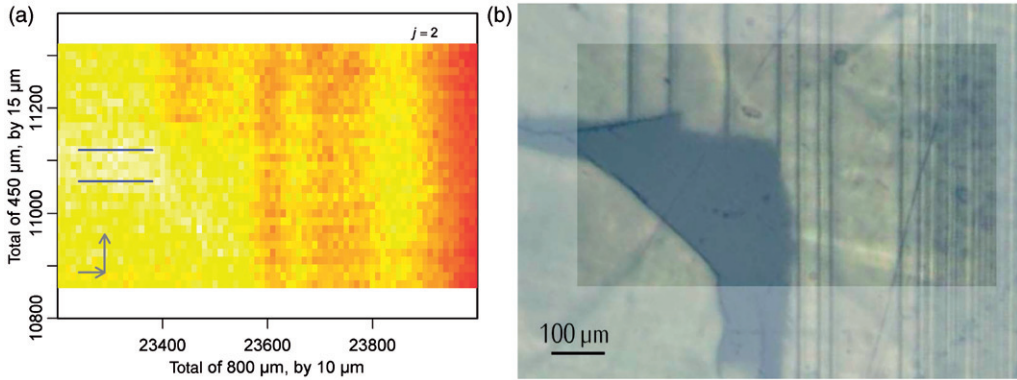
Figure 5. A comparison of the photograph of the scanned area D (5(b)) with one of the extracted SVD components (5(a)). The patterns display matching features. (a) The delinearised rSV2 reveals the domain stripes perpendicular to the probe metallisation. The arrows in the corner project the movement of the positioning stage: from left to right and from bottom to top. (b) A photograph of the scanned area D. We manipulated Figure 3 for better visual comparison with intensity profile in (a) (left).

The configuration A was indeed very similar to the configuration B. The projection of the polarisation of the domains into the axis parallel to the metallisation of the probe altered during the scanning, in both cases. The difference between the configuration B and the configuration A was in altering the optically dense to optically thin domains and their widths. While in the configuration B, the probe field was scanning over slim optically dense stripes ($\varepsilon = 2000$, $d = 7\,\mu$m) in an optically thin 'continuum' ($\varepsilon = 56$, $d > 100\,\mu$m); in the configuration A, the probe field was scanning over slim optically thin stripes ($\varepsilon = 56$, $d = 7\,\mu$m) in an optically dense 'continuum' ($\varepsilon = 2000$, $d > 100\,\mu$m). We performed simulations to get a possible explanation on the matter (Section 3.1).

Additionally, the height profile of the sample was examined in various directions and places within the scanned areas by a differential-interferometric measurement and a surface profiler. These measurements revealed that the flatness of the surface was below 20 nm and 10 nm, respectively.

## 3.1. *Electromagnetic simulations explaining sensitivity*

The CST MicroWave Studio 2009 simulation software environment was employed to get understanding of the underlying processes, including the fact that the spatial resolution was better than expected from the dimensions of the MDP. With respect to the computational time, a model of the MDP with the end-facet dimensions of $50\,\mu$m $\times$ $100\,\mu$m and a sample in a total volume of $2\,$mm $\times$ $2\,$mm $\times$ $5\,$mm were simulated in the frequency range of 10–300 GHz using the automeshing features of the environment. The sample consisted of a large homogeneous block in which a thin stripe was placed, with permittivities $\varepsilon_1$ and $\varepsilon_2$, respectively. The following parameters were common to three different runs: width of the end facet – $50\,\mu$m, thickness of the metallisation – $5\,\mu$m, thickness of the moving 'domain' stripe – $10\,\mu$m. The stripe was displaced across 29 equidistant positions in front of the probe. The permittivity of the probe was kept constant ($\varepsilon_p = 11.4$), while those of the sample structure were altered to simulate various BaTiO$_3$
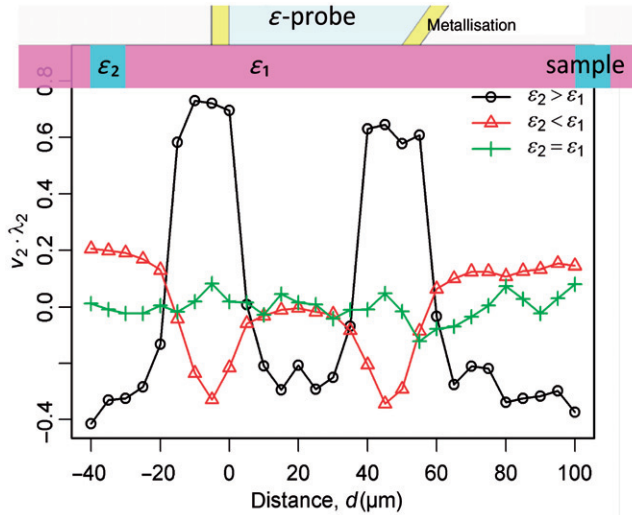
*M. Berta and F. Kadlec*

Figure 6. An overview of the simulation results. The simulations were performed for different combinations of $\varepsilon_1$ and $\varepsilon_2 \in \{60, 300\}$ to model various domains structures and the influence of the automeshing feature of the system. The response of the probe on a domain stripe at various positions was calculated. The functions represent one component of the pulses.

domain combinations and the influence of the automeshing: $(\varepsilon_1, \varepsilon_2) = [(60, 300), (300, 60), (60,60)]$. The changes in the waveforms analysed by SVD are shown in Figure 6 in superposition with a cross-section of the MDP and the sample in the model.

A run with permittivities $\varepsilon_1 = \varepsilon_2 = 60$ was performed to estimate the error influence of the meshing system. This allowed us to estimate the error of the results obtained at other permittivity configurations to $\lesssim 10\%$.

In contradiction to expectations, the domain structure remained hidden for the MDP when optically thin stripes were embedded into the optically dense background (configuration A). That was explained by our electromagnetic transient simulations in which the permittivity of the slim and the wide stripe were altered. The A and B sample-probe configurations were simulated this way. The experimental configuration B corresponded to the permittivity combination $\varepsilon_2 > \varepsilon_1$, and the configuration A corresponded to $\varepsilon_2 < \varepsilon_1$. The permittivity combinations $(\varepsilon_2, \varepsilon_1) = (300, 60)$ and $(\varepsilon_2, \varepsilon_1) = (60, 300)$ did not respond equally in absolute values (Figure 6). In the case of an optically thin stripe surrounded by an optically dense 'continuum', the response of the near-field was weaker. We attribute our inability to resolve sample features in the configuration A to this result.

## 4. Conclusion

We performed measurements on a domain structured $BaTiO_3$ sample under various angles of the polarisation of the probing field with respect to the direction of the domain walls. The aim was to measure the response of the metal-dielectric probe and to find the orientation with optimal sensitivity. The SVD data treatment allowed us to resolve more details and information than a standalone time slices would allow for. In some cases, it can even allow one to define most sensitive time positions for sample scanning at a

fixed time delay. We theoretically analysed the situation in all configurations, and performed electromagnetic simulations to explain lower sensitivity in one of the configurations. The results of the simulations provided a qualitative agreement with our experimental observations.

## Acknowledgements

## References

[1] N. Klein, P. Lahl, U. Poppe, F. Kadlec, and P. Kužel, *A metal-dielectric antenna for terahertz near-field imaging*, J. Appl. Phys. 98 (2005), p. 014910 (5pp).

[2] D.M. Mittleman, *Sensing with Terahertz Radiation*, 1st ed., Springer, Berlin, 2004.

[3] M. Berta, P. Kužel, and F. Kadlec, *Study of responsiveness of near-field terahertz imaging probes*, J. Phys. D Appl. Phys. 42 (2009), p. 155501 (6pp).

[4] A. Dreyhaupt, S. Winnerl, T. Dekorsy, and M. Helm, *High-intensity terahertz radiation from a microstructured large-area photoconductor*, Appl. Phys. Lett. 86 (2005), p. 121114 (3pp).

[5] A. Nahata, D.H. Auston, T.F. Heinz, and C. Wu, *Coherent detection of freely propagating terahertz radiation by electro-optic sampling*, Appl. Phys. Lett. 68 (1996), pp. 150–152.

[6] Z. Li, M. Grimsditch, C.M. Foster, and S. Chan, *Dielectric and Elastic Properties of Ferroelectric Materials at Elevated Temperature*, J. Phys. Chem. Solids 57 (1996), pp. 1433–1438.

[7] M. Schmidt, S. Rajagopal, Z. Ren, and K. Moffat, *Application of singular value decomposition to the analysis of time-resolved macromolecular X-ray data*, Biophys. J. 84 (2002), pp. 2112–2129.

[8] M.E. Wall, A. Rechtsteiner, and L.M. Rocha, *Singular value decomposition and principal component analysis*, in *A Practical Approach to Microarray Data Analysis*, D.P. Berrar, W. Dubitzky, M. Granzow, and M. Norwell, eds., Kluwer, Dorchert, 2003, pp. 91–109.

[9] G. Golub and C. Reinsch, *Singular value decomposition and least squares solutions*, Numer. Math. 14 (1970), pp. 403–420.

[10] R Development Core Team, *R: A Language and Environment for Statistical Computing*, R Foundation for Statistical Computing, Vienna, Austria (2010).

[11] R.B. Cattell, *The scree test for the number of factors*, Multivariate Behav. Res. 1 (1966), pp. 245–276.